Analysis of Low-frequency Drone-Borne GPR for Soil Electrical Conductivity Mapping

Kaijun Wu, Elodie Jacquemin, Loïc Ory, Thibaut Parizel and Sébastien Lambot
Louvain Georadar Research Centre (GPRLouvain), Earth and Life Institute,
Université catholique de Louvain
Louvain-la-Neuve, Belgium
kaijun.wu@student.uclouvain.be,
sebastien.lambot@uclouvain.be

2021 11th International Workshop on Advanced Ground Penetrating Radar (IWAGPR) | 978-1-6654-2253-6/21/$31.00 ©2021 IEEE | DOI: 10.1109/IWAGPR50767.2021.9843145

***Abstract*—In this study, we analysed the low-frequency drone-borne ground-penetrating radar (GPR) and full-wave inversion method for soil electrical conductivity characterization. The sensitivity of parameters (the relative dielectric permittivity ε_r and electrical conductivity σ) is investigated based on the full-wave inversion method. For the full-wave inversion analysis, numerical experiments were conducted within the frequency range of 15-45 MHz. The results show that the soil surface reflexion is more sensitive to the soil electrical conductivity than the soil permittivity to be retrieved using full-wave inversion within this frequency range, with a sensitivity depth of around 0.5 m. Yet, the permittivity also affects the results. For the field experiment, a 5-meter long dipole was mounted on a drone to provide the low frequency range of 15-45 MHz. The measurements were conducted during two different days. The conductivity maps obtained by the drone-borne GPR and by electromagnetic induction (EMI) are presented for comparison. The agreement between the two drone-GPR experiments demonstrated the feasibility of soil conductivity mapping using drone-borne GPR and full-wave inversion. Nevertheless, the conductivity maps were opposite in terms of spatial distributions compared to EMI. This was attributed to the different depth sensitivities of the two methods in relation to the local soil pedology.**

***Index Terms*—Drone, ground-penetrating radar, GPR, full-wave inversion, electrical conductivity, dielectric permittivity, soil conductivity mapping**

I. Introduction

Ground-penetrating radar (GPR) has proven to be one of the promising methods for road inspection [1], [2], tree trunk imaging [3], [4], buried objects detection [5], [6], soil surveys [7]–[9] etc. Nowadays, with the drone technology development, and its features of being low-cost, easy-controlled, high-effective etc. [10], a growing number of new possibilities are available for scientific applications. A commercial GPR was set up on a drone for snow thickness measurement [11], and a time-domain GPR was used for landmine detection [12] etc. For soil properties characterization, we recently proposed a lightweight frequency-domain GPR and used it for soil moisture mapping [13].

The soil electrical conductivity is also an important factor in soil surveys since it depends on the soil texture, clay content, salinity etc. It can be measured by electromagnetic induction (EMI), electrical resistivity tomography (ERT), GPR etc. For instance, the soil conductivity can be estimated from GPR echoes comparison [14] or multi-offset GPR data [15]. On-ground GPR data can be used to retrieve the medium conductivity from multi-scale and full-wave inversion [16]. However, using the off-ground, drone- or air-borne GPR for soil conductivity characterization has remained a challenge.

Parameter sensitivity is important since it determines if it is possible to measure the parameter of interest using a specific technique. In the EMI frequencies, e.g., typically 1-100 kHz, the measurements are sensitive on the soil electrical conductivity and magnetic permeability. The effect of permittivity on EMI is negligible. In addition, focusing on the soil surface reflexion, it is proved that the apparent electrical conductivity can be neglected when it is less than 100 mS/m with the operating frequency higher than 100 MHz [17], making it possible to measure the soil dielectric permittivity with high frequency.

In this study, we analysed the low-frequency drone-borne GPR for soil electrical conductivity mapping. The frequency range we used in this analysis 15-45 MHz. Based on the full-wave inversion method and objective function plots, we conducted numerical experiments to investigate the sensitivity of the surface reflexion to permittivity and conductivity. Secondly, a layered medium model was used to estimate the sensitivity of the surface reflexion with respect to depth. Field measurements were also performed to prove the concept of this low-frequency GPR and full-wave inversion for soil conductivity mapping. We used a 5-meter dipole antenna to provide the frequency range of 15-45 MHz as applied in the numerical experiments. For comparison, we did two drone-borne GPR measurements in two different days (in winter and summer), and EMI maps were provided as well.

II. Full-wave inversion

The inverse problem is defined as a least-squares formulation. It is conducted in the time domain, in order to focus on the medium surface reflexion. The objective function is expressed as:

$$\phi(\mathbf{b}) = (\mathbf{g}^*_{xx}(t) - \mathbf{g}_{xx}(\mathbf{b},t))^\mathsf{T}(\mathbf{g}^*_{xx}(t) - \mathbf{g}_{xx}(\mathbf{b},t)) \quad (1)$$

where $\mathbf{g}^*_{xx}(t)$ is the measured Green's function data (vector N $\times$ 1, where N is the number of data points in the waveform), or the simulated data in the numerical experiments. $\mathbf{g}_{xx}(\mathbf{b},t)$ is the modelled Green's function. t denotes the time. The measured and modelled Green's functions are originally obtained in the frequency domain as $\mathbf{G}^*_{xx}(\omega)$ and $\mathbf{G}_{xx}(\mathbf{b},\omega)$, where ω is the angular frequency. Inverse Fourier transform is used to get data in the time domain as $\mathbf{g}^*_{xx}(t)$ and $\mathbf{g}_{xx}(\mathbf{b},t)$. **b** in the inverse model is the parameter vector. In this paper, **b** = $[\varepsilon_r, \sigma]$ and $[\sigma, h]$ in the numerical and field experiment, respectively. ε_r, σ and h are the relative dielectric permittivity, electrical conductivity and the distance between the antenna aperture and the medium surface. Look-up tables (LUTs) are used for robust and fast inversion.

For the field measurement, the Green's function $G_{xx}^*(\omega)$ is obtained from the far-field radar equation of Lambot et al. [18]. The radar equation accounts for the antenna effect and is expressed as:

$$S_{11} = H_i(\omega) + \frac{H(\omega)G_{xx}^*(\omega)}{1 - G_{xx}^*(\omega)H_f(\omega)} \tag{2}$$

in which S_{11} is measured directly by the vector network analyser (VNA). $G_{xx}^*(\omega)$ is the Green's function defined as the x component of the backscattered electric field for a unit, x-directed electric source for wave propagation in 3D planar layered media. $H_i(\omega)$, $H(\omega)$ and $H_f(\omega)$ are the antenna transfer functions. Specifically, $H_i(\omega)$ is the global reflection coefficient of the antenna for fields incident from the radar reference plane onto the source point. $H_i(\omega) = S_{11}$ in free space conditions where $G_{xx}^*(\omega) = 0$. $H_f(\omega)$ is the global reflection coefficient of the antenna for fields incident from the antenna phase centre (backscattered field) onto the radar reference plane. $H(\omega)$ is the antenna transmitting-receiving response function. The antenna transfer functions are obtained by antenna calibration through several measurements over a lake and solving a matrix equation from the radar equation expressed in Eq.(2). In this study, a lake is used as a relatively large surface is needed as calibrating reflector (a few tens of meters)..

III. Numerical Experiment

In the numerical experiments, we considered two configurations, namely, one- and two-layered medium, respectively, to investigate (1) the sensitivities of the model to the relative dielectric permittivity ε_r and the electrical conductivity σ, and (2) the depth of sensitivity (so-called characterization depth). The frequency range is 15-45 MHz.

A. Model configuration a

The first configuration corresponds to the basic model used for the inversion, with a source above a lossless dielectric half-space. In both simulation and inverse models, the flight height or the distance between the antenna aperture and the medium surface h is set as 6 m in order to analyse the two parameters, ε_r and σ. For the simulation, we present two models in this paper with [ε_r, σ] = [13, 10 mS/m] and [22, 50 mS/m], respectively. For the inverse model, the parameter vector **b** in the objective function was set **b** = [ε_r, σ], and the distance h between the antenna aperture and the medium surface is considered as known (the same as the h in the simulation model), for investigating the sensitivity of the relative permittivity ε_r and the electrical conductivity σ. In addition, in **b**, 0 mS/m $\leq \sigma \leq$ 100 mS/m and $2 \leq \varepsilon_r \leq 26$, and are divided into 101 discrete values, respectively, resulting in 10201 calculations for the LUT.

Fig.1 shows the 15-45 MHz response surfaces of the objective functions in the $\varepsilon_r - \sigma$ parameter plane. As expected, the minimum of the objective function is unique. The sensitivity of the objective function with respect to σ is higher than to ε_r, as the black curve is more flat than the white. Yet, it affects the results when ε_r is too low or too high. Besides, the sensitivity of ε_r is too weak to be estimated by full-wave inversion. These results provide an initial assumption for inverse model, i.e., for the LUT calculation in practice, ε_r can be set to two values (e.g., 10 and 20), to greatly reduce the calculation time.

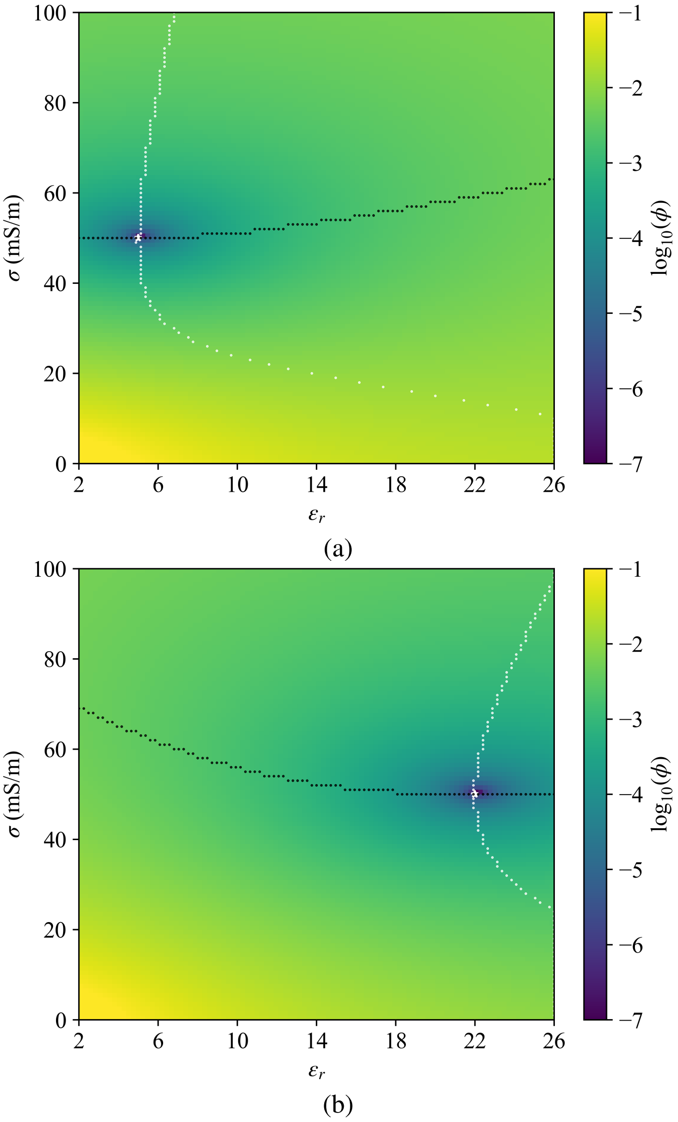

Fig. 1. The 15-45 MHz response surface of the objective function logarithm $\log_{10}(\phi)$ in parameter plane of $\varepsilon_r - \sigma$. The white curve represents the minimum region of the objective function with respect to the conductivity σ. The black curve represents the minimum region of the objective function with respect to the relative dielectric permittivity ε_r.

B. Model configuration b

For configuration b, there is a source situated above a two-layered medium, with the top layer h_1 varying from 0 to 1 m with a step of 0.005 m. The electrical conductivity σ for the upper layer is set to 80 mS/m, and for the lower layer is 50 mS/m. For both the simulation and the inverse model, the distance h between the antenna aperture and the medium surface is 6 m, and the value of ε_r is 13. σ in the inverse model or LUT ranges from 0 to 100 mS/m with a step of 1 mS/m, in order to investigate the layered-medium effects on the estimation of the electrical conductivity σ or its detection depth.

The estimated results as a function of thickness of the top layer h_1 is presented in Fig.2. The "staircase" effect observed results from the discretization of LUT. When the thickness of the top layer h_1 is 0, namely, there is just an half-space, σ of the lower layer is estimated. With h_1 increase, the estimated σ gradually approaches the value of the top layer, and remains afterward. However, the estimated σ is higher than the values of the upper layer 80 mS/m, when h_1 is around between 0.2 m and 0.58 m, but it is still acceptable. The detection depth is indeed affected by the medium permittivity as well as the conductivity, whereas it is generally half meter for most of the soil conditions.

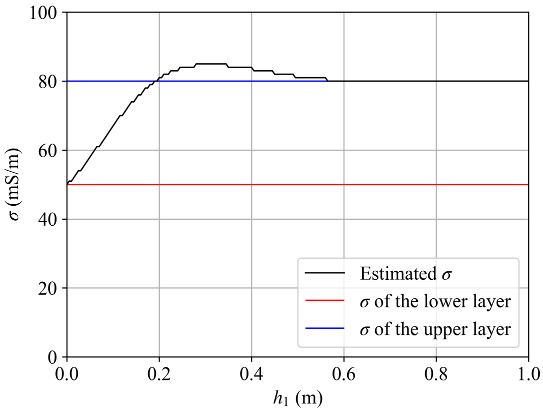

Fig. 2. Estimated electrical conductivity σ as a function of thickness h_1 of the top layer for configuration b.

IV. Field Experiment

The radar and its control system consist of (1) a lightweight VNA (Planar R60, Copper Mountain Technologies, Indianapolis, USA), working as the radar system unit and setting up a stepped-frequency continuous-wave (SFCW) radar; (2) a GPS receiver (GlobalSat BU-353S4) for positioning; (3) an Intel computer stick with a power bank. Python and Javascript programs are developed to remotely control the micro-computer; (4) a smartphone. It launches a hotspot for the micro-computer to connect automatically in order to trigger the remote controlling system installed on the micro-computer; (4) a 5-meter dipole antenna, providing the operating frequency range of 15-45 MHz. The equipment introduced is mounted on the drone, shown in Fig.3. For comparison, we conducted EMI measurement as well in the same site. We used EM38 in the vertical mode.

The calibration, i.e., determining the global reflection and transmission coefficients of the antenna, was conducted over a lake, whose properties are knows (e.g., the temperature and the electrical conductivity). Seven measurements were performed at different flying heights over the lake, with which the antenna characteristic functions are obtained by solving a matrix equation based on Eq.(2). In the inverse model, or the LUT, $\mathbf{b}$ = $[\sigma,\ h,\ \varepsilon]$. 0 mS/m $\leq \sigma \leq$ 100 mS/m with a step of 1 mS/m, 4 m $\leq h \leq$ 8 m with a step of 0.01 m, and ε_r is set to only 2 values, i.e., 10 and 20 as discussed in configuration a, resulting in a 3D LUT and 81002 calculations. Kriging interpolation was used to get the drone-GPR and EMI maps.

The soil conductivity maps obtained by the drone-borne GPR and EMI are shown in Fig.4. Measurements were conducted in winter (Fig.4(a, c)) and summer (Fig.4(b, d)). There is a good agreement between the two maps of the drone-borne GPR (Fig.4(a) and (b)), the soil conductivity becoming higher from the southwest to the northeast. From both drone-GPR and EMI maps, we observe that the soil conductivity is higher in winter than in summer. However, opposite variations are observed from the drone-GPR and EMI maps, and the conductivity measured by EM38 is lower than by GPR. For the drone-borne GPR maps, the high conductivity is the northeast, while for EMI, it is the southwest. The different results between the two techniques is likely to originate from the two different sensitivity depths due to the different detection depth of the methods (0.5 m for GPR and 1.5 m for EMI) in relation to the local soil pedology.

Fig. 3. Prototype drone-borne GPR and drone for soil electrical conductivity mapping.

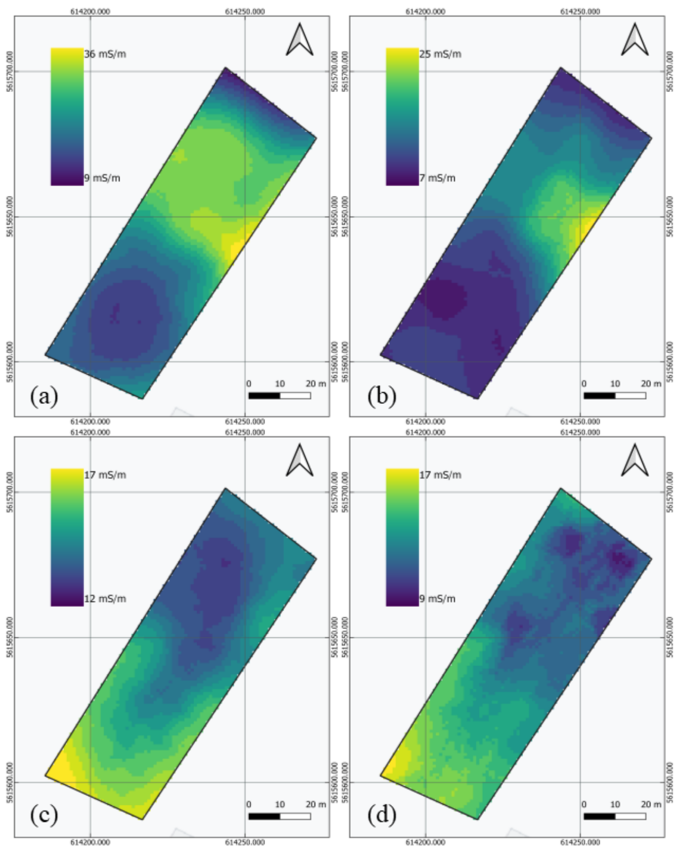

Fig. 4. Soil conductivity map in the Ferme de Lauzelle, Belgium, measured by drone-GPR on (a) 11/25/2020, (b) 06/25/2021, and (c) by EMI (EM38) on 11/25/2020, (d) 06/25/2021. Coordinates are in WGS72/UTM zone 31N (m).

V. Conclusion

In this study, we conducted numerical experiments to investigate the possibility of soil electrical conductivity mapping using low-frequency drone-borne GPR and full-wave inversion method. Specifically, we analysed the sensitivity of the soil permittivity and conductivity within the low-frequency (15-45 MHz) through the objective function. Then we find out the sensitivity depth by building a two-layered medium model. It is concluded that the soil electrical conductivity is sensitive enough to be retrieved using full-wave inversion within the frequency range 15-45 MHz, with detection depth of around 0.5 m. Yet, permittivity still affects the results in that frequency range. Field experiments were also performed. The correspondence between two measurements proved the feasible of soil conductivity mapping using drone-borne GPR and full-wave inversion. The opposite results of EMI would mainly result from the different characterization depths. Our future work will focus on the validation by using other techniques for soil conductivity characterization, e.g., conducting EM38 in the horizontal mode or ERT measurement to obtain a similar characterization depth and scale.

Acknowledgments

This research was funded by the Politique Scientifique Fédérale (BELSPO, Belgium) in the frame of the Research Programme for Earth Observation STEREO III, RAPAS project (contract SR/00/238) and the Fonds de la Recherche Scientifique (FNRS, Belgium).

References

[1] G. Morcous and E. Erdogmus, "Accuracy of ground-penetrating radar for concrete pavement thickness measurement," *Journal of Performance of Constructed Facilities*, vol. 24, no. 6, pp. 610–621, 2010.

[2] A. De Coster, A. Van der Wielen, C. Grégoire, and S. Lambot, "Evaluation of pavement layer thicknesses using gpr: A comparison between full-wave inversion and the straight-ray method," *Construction and Building Materials*, vol. 168, pp. 91–104, 2018.

[3] J. Jezova and S. Lambot, "A dielectric horn antenna and lightweight radar system for material inspection," *Journal of Applied Geophysics*, p. 103822, 2019.

[4] I. Giannakis, F. Tosti, L. Lantini, and A. Alani, "Health monitoring of tree trunks using ground penetrating radar," *IEEE Transactions on Geoscience and Remote Sensing*, vol. PP, pp. 1–10, 2019.

[5] D. Daniels, "A review of gpr for landmine detection," *Sensing and Imaging*, vol. 7, pp. 90–123, 2006.

[6] O. Lopera, E. C. Slob, N. Milisavljević, and S. Lambot, "Filtering soil surface and antenna effects from gpr data to enhance landmine detection," *IEEE Transactions on Geoscience and Remote Sensing*, vol. 45, no. 3, pp. 707–717, 2007.

[7] J. Minet, S. Lambot, E. C. Slob, and M. Vanclooster, "Soil surface water content estimation by full-waveform gpr signal inversion in the presence of thin layers," *IEEE Transactions on Geoscience and Remote Sensing*, vol. 48, no. 3, pp. 1138–1150, 2010.

[8] J. Minet, P. Bogaert, M. Vanclooster, and S. Lambot, "Validation of ground penetrating radar full-waveform inversion for field scale soil moisture mapping," *Journal of Hydrology*, vol. 424-425, pp. 112–123, 2012.

[9] A. P. Tran, M. Vanclooster, M. Zupanski, and S. Lambot, "Joint estimation of soil moisture profile and hydraulic parameters by ground-penetrating radar data assimilation with maximum likelihood ensemble filter," *Water Resources Research*, vol. 50, no. 4, pp. 3131–3146, 2014.

[10] D. Floreano and R. J. Wood, "Science, technology and the future of small autonomous drones," *Nature*, vol. 521, no. 7553, pp. 460–466, 2015.

[11] H. Machguth, O. Eisen, F. Paul, and M. Hoelzle, "Strong spatial variability of snow accumulation observed with helicopter-borne gpr on two adjacent alpine glaciers," *Geophysical Research Letters*, vol. 33, no. 13, 2006.

[12] D. Šipoš, P. Planinšič, and D. Gleich, "On drone ground penetrating radar for landmine detection," in *2017 1st International Conference on Landmine: Detection, Clearance and Legislations, LDCL 2017*, Conference Proceedings, pp. 7–10.

[13] K. Wu, G. A. Rodriguez, M. Zajc, E. Jacquemin, M. Clément, A. De Coster, and S. Lambot, "A new drone-borne gpr for soil moisture mapping," *Remote Sensing of Environment*, vol. 235, p. 111456, 2019.

[14] B. Wu, X. Li, K. Zhao, T. Jiang, Z. Xingming, X. li, L. Gu, and X. Wang, "A nondestructive conductivity estimating method for saline-alkali land based on ground penetrating radar," *IEEE Transactions on Geoscience and Remote Sensing*, vol. PP, pp. 1–10, 2019.

[15] F. Lavoué, R. Brossier, L. Métivier, S. Garambois, and J. Virieux, "Two-dimensional permittivity and conductivity imaging by full waveform inversion of multioffset gpr data: A frequency-domain quasi-newton approach," *Geophysical Journal International*, vol. 197, pp. 248–268, 2014.

[16] D.-S. Feng, C. Cao, and X. Wang, "Multiscale full-waveform dual-parameter inversion based on total variation regularization to on-ground gpr data," *IEEE Transactions on Geoscience and Remote Sensing*, vol. PP, pp. 1–16, 2019.

[17] S. Lambot, L. Weihermüller, J. A. Huisman, H. Vereecken, M. Vanclooster, and E. C. Slob, "Analysis of air-launched ground-penetrating radar techniques to measure the soil surface water content," *Water Resources Research*, vol. 42, no. 11, 2006.

[18] S. Lambot, E. C. Slob, I. D. Van Bosch, B. Stockbroeckx, and M. Vanclooster, "Modeling of ground-penetrating radar for accurate characterization of subsurface electric properties," *IEEE Transactions on Geoscience and Remote Sensing*, vol. 42, no. 11, pp. 2555–2568, 2004.